

Special Section: Nonuniform Flow across Vadose Zone Scales

Core Ideas

- Soil pipes are important features contributing to nonuniform flow in the vadose zone.
- Soil pipe flow and internal erosion is modeled with coupled flow and transport equations.
- Modeling results compare favorably to experimental measurements.

J.L. Nieber, Bioproducts and Biosystems Engineering, Univ. of Minnesota, St. Paul, MN 55108; G.V. Wilson, USDA-ARS, National Sedimentation Lab., Oxford, MS 38655; G.A. Fox, Biological and Agricultural Engineering, North Carolina State University, Raleigh, NC 27695. *Corresponding author (nieber@umn.edu).

Received 16 Sept. 2018.
Accepted 20 Apr. 2019.

Citation: Nieber, J.L., G.V. Wilson, and G.A. Fox. 2019. Modeling internal erosion processes in soil pipes: Capturing geometry dynamics. *Vadose Zone J.* 18:180175. doi:10.2136/vzj2018.09.0175

© 2019 The Author(s). This is an open access article distributed under the CC BY-NC-ND license (<http://creativecommons.org/licenses/by-nc-nd/4.0/>).



Modeling Internal Erosion Processes in Soil Pipes: Capturing Geometry Dynamics

J.L. Nieber,* G.V. Wilson, and G.A. Fox

The flow of water in a soil pipe and the resulting erosion of the soil pipe wall is simulated using a numerical solution of the Reynolds-averaged Navier–Stokes equations coupled with the well-known linear excess shear stress equation and the governing equation for transport of suspended sediment in turbulent flow. The modeling results are compared with an experiment in which the entrance to the soil pipe constructed in a laboratory flume was subjected to a constant head of water in a reservoir. The modeled pipe discharge was in good agreement with the measured results when roughness was imposed on the pipe wall. The temporal growth of the soil pipe was in good agreement with the experimental results when using a soil erodibility coefficient of 0.0025 s/m. Several assumptions were made in model formulation, the most significant being that the soil pipe grows uniformly along its length and that no sediment deposition occurs. Recommendations for future work regarding these assumptions as well as others are discussed.

Abbreviations: CFD, computational fluid dynamics.

Soil pipe flow is an extreme case of nonuniform flow that involves flow through preferential flow paths at velocities sufficient to erode the inner walls. For this reason, Beven and Germann (1982) concluded that soil pipes are distinguished from macropores by the appearance of a water-sculptured form, i.e., evidence of internal erosion (Jones, 2010). In fact, flow velocities in soil pipes have been shown by dye tracing to be in the range of streamflow velocities and, like streams, the flows can be highly turbulent (Wilson et al., 2016; Zhou et al., 2016). Wilson et al. (2018) stated in a summary of hydrodynamic processes involved in pipe flow that “pipe flow velocities can exceed surface flow velocities because the flow is concentrated into a small conduit whereas surface flow can spread out with vegetation and other roughness features slowing the surface velocity.” As a result of these large pipe flow velocities, shear forces readily exceed the frictional strength binding soil, which results in detachment of particles and aggregates. The resultant internal erosion not only enlarges the pipe such that it can handle greater flow velocities but also can enhance the pipe network’s contributing area and connectivity, which Wilson et al. (2016) termed a self-propagating process.

Water pressures within soil pipes are highly dynamic and spatially variable, with changes as high as tens of centimeters within minutes and these elevated pressures being sustained for hours to days (Wilson et al., 2017). Thus, the flow velocities are extremely variable spatially and temporally (Bernatek-Jakiel et al., 2017), being dependent on the pipe size, landscape position, season, internal roughness, sinuosity, and connectivity of the soil pipe (Sidle et al., 1995, 2001; Nieber and Sidle, 2010; Wilson 2009, 2011; Wilson et al., 2017). As a result of the high flow velocities, sediment detachment can exceed the transport capacity of the soil pipe, which can result in temporary clogging of the pipe. Wilson (2009, 2011) noted that pipe flow rates, even under conditions of a steady inflow rate, exhibit short-duration flow stoppages followed by surges in flow rate and sediment concentrations due to clogging. Such blockages in pipes can result in sudden pressure buildups within the pipe and in the adjacent soil (Wilson and Fox, 2013). Wanger et al. (2019) simulated pipe plugs in the laboratory and showed that the critical pressure for plug

removal was dependent on the plug properties (texture and bulk density), plug size, and time (wetting-up period).

An additional complexity is the observation that pipes can flow partially full, thus not all the pipe periphery is acted on by the shear forces of the flowing water. Given these complexities, it is no wonder that Bernatek-Jakiel and Poesen (2018) found in their literature review on piping that no water erosion model includes piping. This is despite their finding that piping has been reported in “almost all climatic zones of the world,” all landforms, 20 of the 28 soil types, and “almost every soil texture.” Despite the ubiquitous nature of piping, very little work has been done on erosion by pipe flow (Fox and Wilson, 2010). In a review on internal erosion by pipe flow, Wilson et al. (2018) reported that only 7% of the papers published in the last two decades on soil pipes dealt with sediment transport. They found that “none were controlled experimental studies on the processes involved, such as mechanisms of particle or aggregate detachment from pipe walls or transport, filtering (physical entrapment) or sorption/flocculation and sedimentation of the particles.”

Beven and Germann (2013) reviewed the progress made on preferential flow in the last 30 yr since their classic paper (Beven and Germann, 1982) on macropore flow. Despite the enormous body of work since that time on macropore flow and preferential flow in general, they concluded that “the topic has still not received the attention that its importance deserves.” Even with the proliferation of research on preferential flow in the last three decades, Wilson et al. (2018) found that only 1% of the studies on macropores in the last two decades “dealt to any degree with particle detachment and sediment transport.” It is no wonder that erosion models do not include pipe flow processes; given the scarcity of studies on the processes involved, it is difficult to mathematically represent processes that are so poorly understood and quantified. Wilson et al. (2018) supplemented the literature on sediment detachment and transport in macropores and soil pipes with extensive research conducted on streams and man-made (industrial) pipes to better understand the processes involved. From this review, they recommended that future research needs to: “develop mechanistic mathematical expressions for describing soil detachment within soil pipes that account for seepage gradient forces and effects of gravity on pipe walls and roofs; and develop models capable of simulating the mechanics of sediment detachment, transport, and deposition in soil pipes, and associated changes in the geometry of soil pipes, as well as collapse of pipes to form gullies.”

The first step in modeling sediment transport in soil pipes is to model the pipe flow. Considerable work has been conducted on modeling macropore flow (Gerke, 2006; Jarvis, 2007; Beven and Germann, 2013). The most common approach for modeling pipe flow is the application of Richards’ equation by treating the soil pipe as a highly conductive porous medium rather than a linear void and manipulating the hydraulic properties of the pipe region (Nieber and Sidle, 2010; Wilson et al., 2013). Some of the problems with the Richards equation approach are: (i) flow may

be turbulent and therefore invalidate strict use of Darcy’s law for flow in the pipe; (ii) modeling the linear void as a porous material requires a hypothetical description of the hydraulic properties for the pipe region, water content $\theta(h)$ and hydraulic conductivity $K(h)$ (e.g., Gerke and van Genuchten, 1993; Nieber and Sidle, 2010), which is a choice of expedience; (iii) physical and hydraulic nonequilibrium exists between the soil matrix and soil pipe; (iv) pipe geometries and water levels (i.e., partially full) in soil pipes change dynamically, therefore changing boundary conditions for the flow domain; and (v) parameter values vary spatially and temporally. Such problems, among many others, led Beven and Germann (2013) to conclude that the Richards approach is not an adequate representation of the flow processes, but they acknowledged that “there is still not an adequate physical theory linking all types of flow.”

Beven and Germann (2013) proposed “radical alternatives” for modeling preferential flow, and there they were referring to the broad range of flows that are considered to be preferential. With regard to the preferential flow phenomenon associated with soil pipe flow, the review by Wilson et al. (2013) concluded that “future modeling efforts should ... incorporate internal erosion and sediment transport” in existing pipe flow models. To follow up on that conclusion, the objectives of this study were to test a new modeling strategy for simulating internal erosion of pipes based on measured sediment transport from soil pipes studied under controlled laboratory experiments by Wilson (2009, 2011).

Methods

Laboratory Experiments

To provide a more complete context for the modeling work presented here, we provide a brief overview of the experiments conducted by Wilson (2011). The experiments were conducted on two soil textures represented by Providence silt loam soil (a fine-silty, mixed, active, thermic Oxyaquic Fragiudalf) and Smithdale loam soil (a fine-loamy, siliceous, subactive, thermic Typic Hapludult), both collected in the area of northern Mississippi. The soils were packed moist to a dry bulk density of 1.3 g cm^{-3} to a depth of 20 cm in an acrylic plastic flume 140 cm long and 100 cm wide with a removal rod planted along the midplane of the packed soil. The removal of the rod created an open conduit in the soil and this conduit is the model soil pipe. Here we show the results for one of the experiments conducted with the Providence silt loam soil. To gain a full appreciation for the wide range of conditions studied in the experiments, see Wilson (2011). For those experiments, one end of the flume was exposed to a reservoir of water, while the other end was open to the atmosphere and set up to measure pipe flow. During the experiments, the water level in the reservoir was held at a height of 0.15 m above the pipe opening. Two replicates of the experiment were conducted for each soil and for several initial pipe diameters.

For each experimental run, the soil was packed around the metal rod that extended the length of the flume at a height of 6 cm above the base of the flume. After packing, the metal rod was removed to

leave behind an open pipe in the soil, extending from the flume constant-head reservoir to the outlet. Different rod diameters were used in different experiments: 2, 4, 6, 8, and 10 mm. Note that the soil in the flume was separated from the water in the reservoir by an acrylic plastic wall that had an 89-mm hole centered 6 cm above the base of the flume. The constructed soil pipe for each experiment was exposed to the reservoir through the center of this 89-mm hole. After setting up the soil and soil pipe for each experiment, the 89-mm hole in the wall was plugged while the reservoir was filled to the specified height. Then the plug was removed to start the experiment. The discharge at the exit point of the pipe was measured along with samples of water taken to measure the sediment flux and sediment concentration in the discharge water. For all of the experiments conducted, the duration lasted a maximum of 30 min—less time if the soil above the pipe collapsed. Here we discuss the experimental results for the soil pipe produced by the 6-mm rod.

The discharge and sediment concentration as a function of time at the pipe discharge point for one of the 6-mm-diameter pipe replicated experiments are illustrated in Fig. 1a, while the pipe discharge and the suspended sediment flux for the same replicate are plotted vs. time in Fig. 1b. The sediment concentration distribution with time shown in Fig. 1a is similar to the sediment concentration distribution found for the other replicate (graph not shown; see Wilson, 2011), but the pipe discharges for the two replicates were quite different, with the discharges for the second replicate being almost an order of magnitude larger. The larger measured discharge for the second replicate cannot be explained based on hydraulic theory, and Wilson (2011) did not provide an explanation for the large difference. It will be shown below that the pipe discharge for the replicate shown in Fig. 1a can be explained using hydraulic theory, so that is the case that will be examined in the present analysis.

From Fig. 1a and 1b it can be observed that while the erosion rate increases as the soil pipe diameter increases (Fig. 1b), the rate of increase in sediment flux is smaller than the rate of increase in discharge. This then leads to a dilution effect, resulting in the observed decrease in suspended sediment concentration with time shown in Fig. 1a.

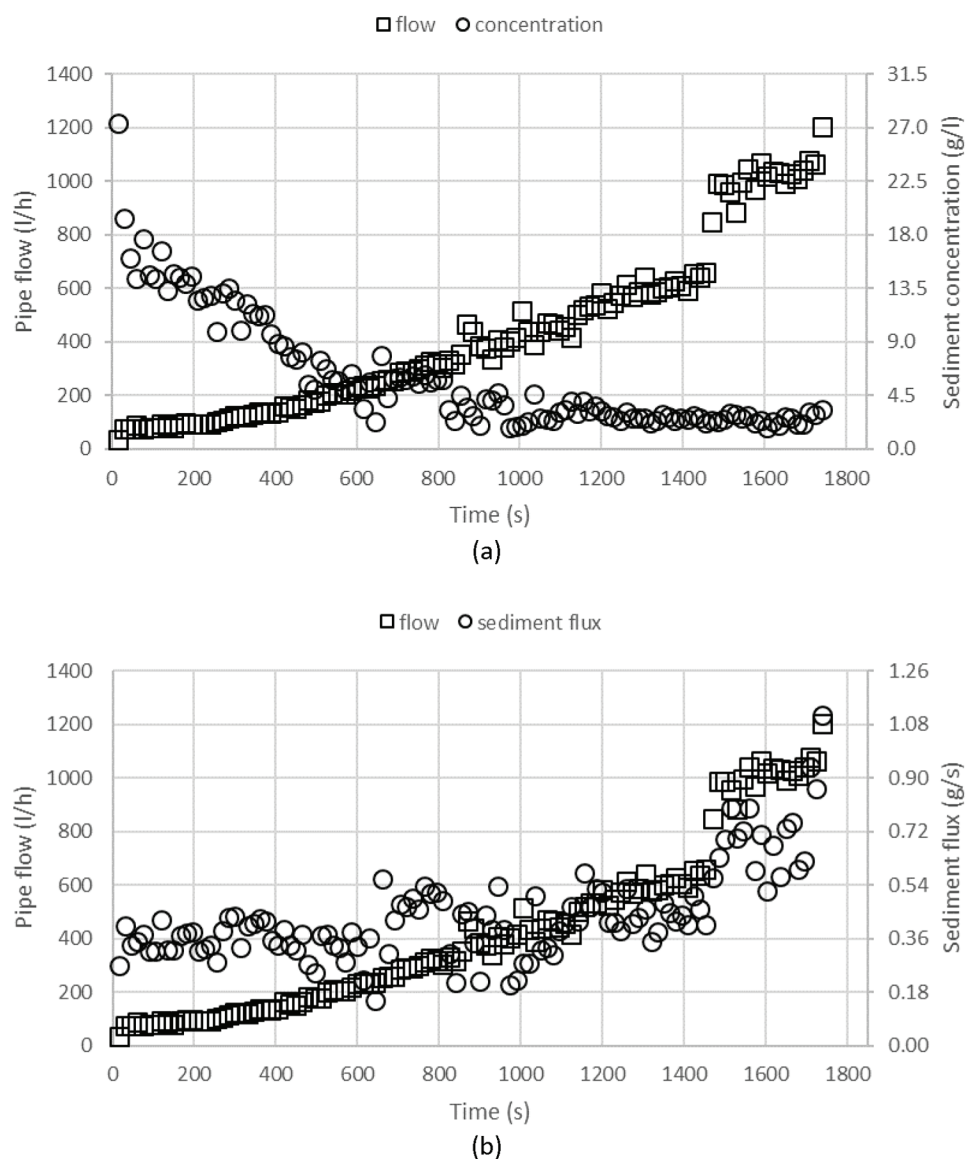


Fig. 1. (a) Pipe flow and pipe flow suspended sediment concentration vs. time for one of the replicated experiments reported by Wilson (2011) for the Providence soil with the initial pipe diameter of 6 mm, and (b) pipe flow and pipe flow suspended sediment flux vs. time for the same experiment.

At the end of the experiment for the first replicate, the soil pipe was dissected to measure the pipe diameter at 10-cm intervals along the pipe. A plot of the measured pipe diameter vs. distance along the pipe is shown in Fig. 2. The diameter is largest near the entrance, with a general trend of decreasing diameter toward the outlet. However, the trend in diameter along the length of the pipe is not fully monotonically decreasing. This information about pipe diameter variation along the length of the pipe is utilized below in the modeling of the flow, soil erosion, and sediment transport.

Modeling

For the pipe flows reported by Wilson (2011), the fluid readily transitions into the turbulent range; calculated values of the Reynolds number range from 2100 for the 6-mm-diameter pipe

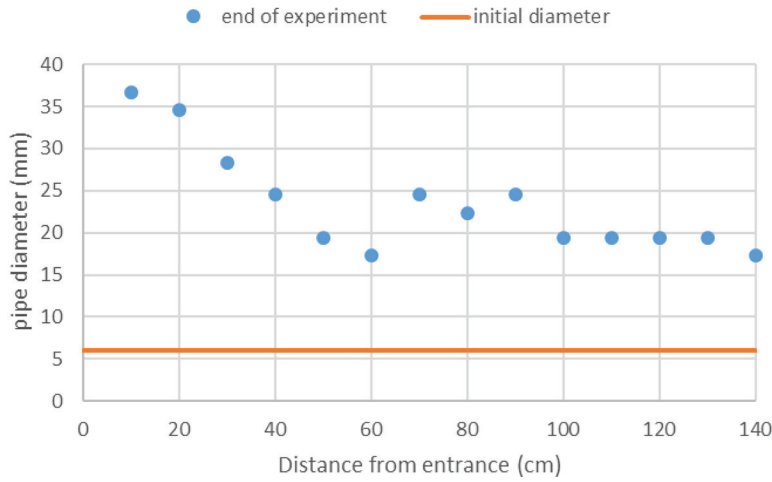


Fig. 2. Distribution of pipe diameter along the length of the soil pipe at the end of the experiment. The pipe diameter was measured by dissection of the soil in the laboratory flume. The initial diameter of the soil pipe was made with a steel rod and it was assumed the diameter was uniform along the length of the flume.

at the beginning of the experiment to >18,000 for the 24-mm-diameter pipe at the end of the experiment. A brief overview of the derivation of the governing equations needed to simulate the turbulent flow in a soil pipe is now presented.

The equations governing the flow of water in a soil pipe are represented by the three-dimensional Navier–Stokes equations:

$$\rho(\nabla \cdot \mathbf{V}) = 0 \quad [1.1]$$

$$\rho \frac{\partial \mathbf{V}}{\partial t} + \rho(\mathbf{V} \cdot \nabla) \mathbf{V} = -\nabla p \mathbf{I} + \rho \mathbf{g} + \nabla \cdot [\mu \nabla \mathbf{V} + (\nabla \mathbf{V})^T] \quad [1.2]$$

where ρ is fluid density; \mathbf{V} is the vector of velocity composed of components u_x , u_y , and u_z ; p is fluid pressure; \mathbf{g} is the vector of gravitational acceleration composed of components g_x , g_y , and g_z ; μ is the dynamic viscosity of water; and \mathbf{I} is the identity matrix.

When the water flow in the soil pipe transitions into turbulent flow, the velocity \mathbf{V} and the pressure p can be expressed by time-averaged terms and random terms:

$$\left. \begin{aligned} \mathbf{V} &= \bar{\mathbf{V}} + \mathbf{V}' \\ p &= \bar{p} + p' \end{aligned} \right\} \quad [2]$$

where $\bar{\mathbf{V}}$ and \bar{p} are the time-averaged velocity and pressure, respectively, and \mathbf{V}' and p' are the random terms for velocity and pressure, respectively.

Substituting these into Eq. [1.1] and [1.2] and time averaging yields

$$\rho(\nabla \cdot \bar{\mathbf{V}}) = 0 \quad [3.1]$$

$$\begin{aligned} \rho \frac{\partial \bar{\mathbf{V}}}{\partial t} + \rho(\bar{\mathbf{V}} \cdot \nabla) \bar{\mathbf{V}} + \nabla \cdot \overline{\rho(\mathbf{V}' \otimes \mathbf{V}')} = \\ -\nabla \bar{p} \mathbf{I} + \rho \mathbf{g} + \nabla \cdot \mu [\nabla \bar{\mathbf{V}} + (\nabla \bar{\mathbf{V}})^T] \end{aligned} \quad [3.2]$$

where \otimes is the outer vector product. To get this result, all random terms that appear alone when relations Eq. [2] are substituted into Eq. [1.1] and [1.2] will zero out when the time-averaging process takes place. The only term with random components that survives the averaging is the third term on the left, that is, $\nabla \cdot \overline{\rho(\mathbf{V}' \otimes \mathbf{V}')}$, because the product in the terms is always positive. This term is referred to as the Reynolds stresses and is associated with the momentum transfer occurring due to the turbulent flow components. Equation [3.2] contains two stress terms, the molecular shear stress given by the last term on the right, and the Reynolds stress term. Equations [3.1] and [3.2] are referred to as the Reynolds-averaged Navier–Stokes equations. When the turbulent flow is steady state, that is, $\bar{\mathbf{V}}$ does not change with time, the time derivative in Eq. [3.2] also becomes zero. For the present study, $\bar{\mathbf{V}}$ was taken to be independent of time, so $\partial \bar{\mathbf{V}} / \partial t = 0$.

Equations [3.1] and [3.2] constitute a total of four equations with seven unknowns: \bar{u}_x , \bar{u}_y , \bar{u}_z , \bar{p} , u'_x , u'_y , and u'_z . Thus additional equations are needed to be able to close the mathematical problem. A number of methods have been developed in the computational fluid dynamics community to solve this problem; see the detailed description given by Wilcox (2006). In general, these methods replace the Reynolds stress term with equations that contain the mean flow field velocity and pressure. One such approach is the k – ω method (e.g., Wilcox, 2008), where k refers to the turbulent kinetic energy and ω refers to the dissipation rate of the turbulent kinetic energy. Conservation equations and constitutive relations for each, k and ω , are written in terms of the mean velocity field. The addition of these equations or relations provides closure to the problem.

The Reynolds-averaged Navier–Stokes equations using a k – ω formulation are given by the following set of equations (recall that $\partial \bar{\mathbf{V}} / \partial t = 0$ for the application here):

$$\rho(\nabla \cdot \bar{\mathbf{V}}) = 0 \quad [4.1]$$

$$\rho(\bar{\mathbf{V}} \cdot \nabla) \bar{\mathbf{V}} = -\nabla \bar{p} \mathbf{I} + \rho \mathbf{g} + \nabla \cdot (\mu + \mu_T) [\nabla \bar{\mathbf{V}} + (\nabla \bar{\mathbf{V}})^T] \quad [4.2]$$

$$\rho(\bar{\mathbf{V}} \cdot \nabla) k = \nabla \cdot [(\mu + \mu_T \sigma_k) \nabla k] + P_k - \beta_k \rho \omega k \quad [4.3]$$

$$\rho(\bar{\mathbf{V}} \cdot \nabla) \omega = \nabla \cdot [(\mu + \mu_T \sigma_\omega) \nabla \omega] + \alpha \frac{\omega}{k} P_k - \rho \beta_\omega \omega^2 \quad [4.4]$$

$$\mu_T = \rho \frac{k}{\omega} \quad [4.5]$$

$$P_k = \mu_T \left[\nabla \bar{\mathbf{V}} : [\nabla \bar{\mathbf{V}} + (\nabla \bar{\mathbf{V}})^T] - \frac{2}{3} (\nabla \cdot \bar{\mathbf{V}})^2 \right] - \frac{2}{3} \rho k \nabla \cdot \bar{\mathbf{V}} \quad [4.6]$$

where $\bar{\mathbf{V}}$ is the time-averaged velocity vector (m s^{-1}) composed of the x , y , and z components of velocity, \bar{u}_x , \bar{u}_y , and \bar{u}_z respectively; \bar{p} is the time-averaged pressure (Pa); ρ is the fluid density (kg m^{-3}); k is the specific turbulent kinetic energy ($\text{m}^2 \text{s}^{-2}$); ω is

the specific dissipation rate of turbulent kinetic energy (s^{-1}); P_k is the specific production rate for turbulent kinetic energy ($W\ m^{-3}$); μ_T is the turbulent viscosity (Pa s);

$$\beta_\omega = \beta_{\omega,0} \frac{1+70\chi_w}{1+80\chi_w};$$

$$\chi_w = \left| \frac{\Omega_{ij}\Omega_{jk}S_{ki}}{(\beta_{\omega,0}\omega)^3} \right|;$$

$$\beta_k = \beta_{k,0}f_\beta;$$

$$f_\beta = \begin{cases} 1 & \chi_k \leq 0 \\ \frac{1+680\chi_k^2}{1+400\chi_k^2} & \chi_k = \frac{1}{\omega^3}(\nabla k \cdot \nabla \omega) \end{cases};$$

$$\Omega_{ij} = \frac{1}{2} \left(\frac{\partial \bar{u}_i}{\partial x_j} - \frac{\partial \bar{u}_j}{\partial x_i} \right);$$

$$S_{ij} = \frac{1}{2} \left(\frac{\partial \bar{u}_i}{\partial x_j} + \frac{\partial \bar{u}_j}{\partial x_i} \right);$$

and α , σ_ω , σ_k , $\beta_{k,0}$, and $\beta_{\omega,0}$ are all dimensionless turbulence model parameters.

Equations [4.1–4.6] represent seven independent equations (note that Eq. [4.2] is composed of three independent equations, one for each coordinate direction) with seven unknowns: \bar{u}_x , \bar{u}_y , \bar{u}_z , \bar{p} , k , ω , and P_k .

Equation [4.1] is the conservation of mass equation, Eq. [4.2] is the time-averaged momentum equation for turbulent flow, while Eq. [4.3–4.6] represent the conservation equations and constitutive relations for specific turbulent kinetic energy (k), specific turbulent kinetic energy dissipation rate (ω), and specific turbulent kinetic energy production rate (P_k). These equations apply to the turbulent boundary layer, which starts at a small distance δ from the pipe wall. From the pipe wall ($r = r_p$) to $r = r_p - \delta$, the flow is laminar, and this interval constitutes the laminar sublayer with an assumed linear velocity profile.

The boundary conditions for the turbulent flow equations are given by

$$p = \rho g H \quad \text{at } x = 0 \quad (\text{pipe entrance}) \quad [5.1]$$

$$p = 0 \quad \text{at } x = 1.4 \text{ m} \quad (\text{pipe exit}) \quad [5.2]$$

$$\bar{u}_x = \bar{u}_{x\delta}, \quad \bar{u}_y = 0, \quad \bar{u}_z = 0 \quad \text{at } r = (r_p - \delta) \quad (\text{edge of laminar sublayer}) \quad [5.3]$$

where H is the pressure head at the pipe entrance, $\bar{u}_{x\delta}$ is the velocity at the interface of the turbulent boundary layer with the laminar sublayer, and r_p is the pipe radius.

The thickness of the laminar sublayer is a variable in the computations and not a preset parameter. It is calculated based on the

requirement that the velocity profile in the laminar sublayer is proportional to the wall shear stress, τ_w . This velocity profile is expressed by (Munson et al., 2013, p. 422–423)

$$\bar{u}_{xls} = \frac{\tau_w (r_p - r)}{\mu} \quad (r_p - \delta) \leq r \leq r_p \quad [6]$$

where \bar{u}_{xls} is the velocity in the laminar sublayer, and $\bar{u}_{xls} = \bar{u}_{x\delta}$ at $r = (r_p - \delta)$.

The modeling of soil particle detachment and transport of suspended sediment in the soil pipe is based on the governing equation for sediment transport accounting for the turbulent transfer of sediment from the soil pipe wall into the main stream of water flow through the soil pipe, where the erosion of the soil pipe wall is given by the well-known excess shear equation (Partheniades, 1965). Assumptions made for the modeling are:

1. The potential to exceed the sediment transport capacity of the flow can be neglected, and therefore no sediment deposition occurs.
2. The effect of sediment concentration on fluid properties and the interaction of suspended particles on erosion rate and particle dispersion can be neglected.
3. Flow for any given pipe diameter is steady. Because pipe flow can be turbulent, this means that the flow is steady on a time-averaged basis.
4. The pipe is assumed to have a uniform diameter and remains straight along its length even while the diameter expands due to erosion.

The equation for the transport of suspended sediment is

$$\nabla \cdot (-D_T \nabla \bar{c}) + \bar{\mathbf{V}} \cdot \nabla \bar{c} = 0 \quad [7]$$

where D_T is the turbulent dispersion coefficient ($m^2\ s^{-1}$), and \bar{c} is the time-averaged suspended sediment concentration ($kg\ m^{-3}$). The boundary conditions for sediment transport are

$$-D_T \frac{\partial \bar{c}}{\partial x} + \bar{u} \bar{c} = 0 \quad \text{at } x = 0 \quad (\text{pipe entrance}) \quad [8.1]$$

$$D_T \frac{\partial \bar{c}}{\partial x} = 0 \quad \text{at } x = 1.4 \text{ m} \quad (\text{pipe exit}) \quad [8.2]$$

$$D_T \frac{\partial \bar{c}}{\partial r} = q_s \quad \text{at } r = r_p \quad (\text{pipe wall}) \quad [8.3]$$

where q_s ($kg\ m^{-2}\ s^{-1}$) is the source term for suspended sediment production as a result of wall shear, and $r = (y^2 + z^2)^{1/2}$ is the radial distance from the central axis of the pipe. The source term is given by the well-known excess shear stress equation (Partheniades, 1965):

$$q_s = k_{eros} \left(\mu \frac{\partial \bar{u}_x}{\partial r} \Big|_{r=r_p} - \tau_{crit} \right) \quad [9]$$

where k_{eros} is the soil erodibility coefficient ($s\ m^{-1}$), μ is the dynamic viscosity (Pa s), and τ_{crit} is the critical shear stress (Pa). The first term in the parentheses in Eq. [9] is the wall shear stress, τ_w .

The system of Eq. [4] and [7] with the associated boundary conditions (Eq. [5] and [8]) and associated erosion rate (Eq. [9]) are solved by the finite element method using the COMSOL-MP CFD module (COMSOL, 2018), Version 5.4. The values of the dimensionless turbulent flow parameters, α , σ_ω , σ_k , $\beta_{k,o}$, and $\beta_{\omega,o}$, were set as $\alpha = 0.52$, $\sigma_\omega = 0.5$, $\sigma_k = 0.5$, $\beta_{\omega,o} = 0.133$, and $\beta_{k,o} = 0.166$. Most of these values are the default values set with the COMSOL CFD module and are values the COMSOL developers have tested to show that they yield optimal results. However, in this case, $\beta_{\omega,o}$ and $\beta_{k,o}$ were set to slightly larger values to be able to better match the pipe discharge values calculated with the Darcy–Weisbach pipe flow equation.

Note that the approach used here is to solve the equations for steady-state conditions for a series of sequentially larger pipe diameter configurations. The steps in this solution procedure are as follows.

The solution of the turbulent flow field for a given pipe diameter configuration is derived for a given finite element grid. An example grid is shown in Fig. 3, where we take advantage of the plane of symmetry (solve for only one half of the pipe) to save on memory and computational time. Note that this flow domain pertains only to the soil pipe and does not include the soil matrix surrounding the soil pipe. This grid is composed of triangular prism elements in the central core of the pipe and hexahedral elements within the boundary layer portion of the pipe. The boundary layer elements are specified to be very refined in the region close to the pipe wall to provide high-resolution discretization of the turbulent boundary layer. The solution provides the velocity and pressure distribution within the turbulent boundary layer ($0 \leq r \leq r_p - \delta$) and determines the thickness of the laminar sublayer.

The boundary conditions for pipe flow are no slip on the walls of the pipe, atmospheric pressure at the pipe outlet, and a specified pressure of 1471 Pa (0.15-m pressure head) at the inlet of the pipe. Typically, the velocity profile in a turbulent boundary layer in a cylindrical conduit is assumed to be one of two empirical equation

forms, a logarithmic function or a power law function with an exponent of 1/7 (Munson et al., 2013; p. 423). Here the initial guess for the velocity profile was the 1/7th power law velocity, with an initial guess at the maximum velocity, $u_{x,\max}$. The form of this function is

$$\bar{u}_x = u_{x,\max} \left[1 - \frac{(y^2 + z^2)^{1/2}}{r_p} \right]^{1/7} \quad [10]$$

Using this initial guess at the turbulent velocity profile, the solution is iterated within the numerical solution until convergence yields the distribution of pressure, velocity, turbulent kinetic energy, and rate of turbulent kinetic energy dissipation along the pipe. The final velocity distribution is used to compute the pipe discharge at the entrance and exit of the pipe. Using this velocity profile, the advection–dispersion equation (Eq. [7]) along with the boundary conditions, Eq. [8], and the erosion rate, Eq. [9], is solved to determine the erosion from the pipe walls and transport of resulting suspended sediment to the pipe outlet.

The solutions were obtained for the case of the initial pipe diameter of 6 mm, and then for five sequentially larger diameters including 8, 12, 16, 20, and 24 mm as the pipe enlarges by internal erosion. It was assumed that the pipe enlarges uniformly along the length of the pipe, whereas it is known from observations made at the end of these experiments that this is not the case. As expected, the numerical solutions showed that the shear stress distribution on the wall of the pipe was very high near the pipe entrance but decreased rapidly to a fairly uniform value. This difference in shear stress would imply that the pipe should grow faster in the upstream end of the pipe. This difference was neglected, however, in the present analysis.

For each pipe diameter, the flow field was computed by solution of Eq. [4–6], and then for the soil erosion and suspended sediment transport by solution of Eq. [7–8] with Eq. [9]. The solution to these equations provides the average erosion rate along the pipe wall, and this erosion rate is used to compute the time required for the pipe to enlarge from one pipe diameter (D_1) to the next (D_2) in the series. This time is calculated as

$$\Delta t = \frac{L \rho_d \pi (D_2^2 - D_1^2)}{4 \bar{E}} \quad [11]$$

where D_1 and D_2 are the beginning and end pipe diameters (m) during a given time interval, L (m) is the length of the pipe, ρ_d is the dry bulk density of the soil composing the pipe wall (kg m^{-3}), and \bar{E} is the average erosion rate (kg s^{-1}) along the pipe wall during the time interval. The accuracy of this approach depends entirely on the increment in pipe diameter used for the calculations. Smaller increments will lead to more accurate results.

The flow computed from the computational fluid dynamics (CFD) solution was checked using the well-known Darcy–Weisbach equation:

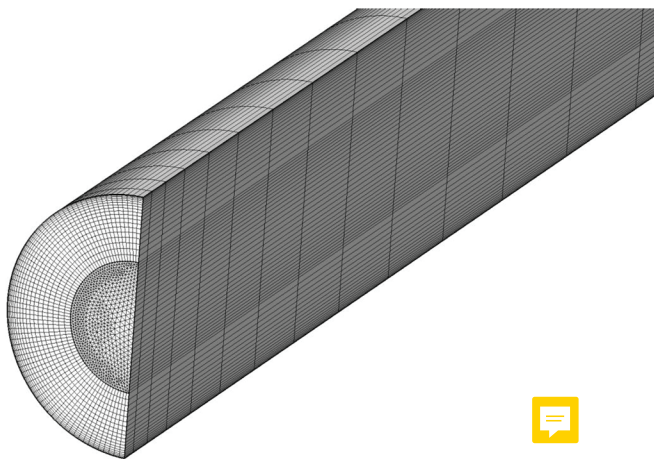


Fig. 3. Finite element grid for the 24-mm-diameter soil pipe, taking advantage of the symmetry in the pipe flow and sediment transport. The grid is composed of triangular prism elements in the core of the pipe flow, and composed of hexahedral elements within the boundary layer of the pipe flow.

$$Q = \left(\frac{H}{L} \frac{\pi^2 \mathbf{g}}{8 f D^5} \right)^{1/2} \quad [12]$$

where $D = 2r_p$ is the pipe diameter and f is the friction factor approximated using the Haaland equation (Haaland, 1983):

$$f = \left\{ -1.8 \log_{10} \left[\left(\frac{\varepsilon}{3.7 D} \right)^{1.11} + \frac{6.9}{R_c} \right] \right\}^{-2} \quad [13]$$

where $R_c = 4\rho Q/\mu\pi D$ is the Reynolds number for the flow, and ε is the pipe wall roughness (m).

Results

In the first set of simulated results presented here, it was assumed that the pipe wall was smooth, i.e., $\varepsilon = 0$. The parameters set for the numerical solution are summarized in the first row of Table 1. Note that the dispersion coefficient, D_T , affects the distribution of sediment across the pipe cross-section but does not affect the mean sediment concentration in the flow or the erosion rate.

The velocity distributions within the turbulent part of the boundary layer across the diameter of the pipe at two locations, the pipe entrance and the pipe exit, are shown in Fig. 4 for the initial state when the diameter pipe is 6 mm. The velocity distribution is nearly uniform at the entrance of the pipe. This results because the flow enters the pipe nearly uniformly across the pipe cross-section. At the outlet, the velocity distribution is very close to the power law velocity profile (not shown here) given by Eq. [10]. A similar velocity profile was calculated for the different diameters of the pipe produced sequentially as a result of pipe wall erosion.

The distribution of shear stress along the wall for the initial soil pipe state with 6-mm diameter is illustrated in Fig. 5. The shear is maximum near the entrance where the velocity profile has very high gradients near the wall and becomes essentially a constant within about 0.20 m of the pipe entrance. A similar shear stress profile was calculated for the different diameters of the pipe produced sequentially as a result of pipe wall erosion.

The wall shear stress profiles and velocity distributions associated with each discrete pipe diameter were then used in the solutions to Eq. [7–9] to obtain the wall erosion rate, \bar{E} , which was then used in Eq. [11] to determine the time increment required for the pipe to increase in diameter from D_1 to D_2 .

Computing the pipe wall erosion rate requires estimation of the erodibility coefficient, k_{eros} , and the critical shear, τ_{crit} . Using a combination of features for the slot erosion test and the hole erosion test as described by Wan and Fell (2004), Wilson (2011) estimated the value of k_{eros} to be 0.035 s m^{-1} and a τ_{crit} value between 0 and 0.007 Pa for the Providence soil. For the modeling presented here, τ_{crit} was taken as 0.005 Pa. However, using the modeled values of wall shear stress (ranging from 1.55 to 6.08 Pa) for each simulated pipe diameter, a value of $k_{\text{eros}} = 0.00195 \text{ s m}^{-1}$ was found to produce the observed time evolution of pipe diameter growing from 6 to 24 mm within 30 min, the time observed for the pipe to enlarge to the average diameter of about 23.4 mm. This value of k_{eros} is about 1/20 of the value estimated by Wilson (2011) for the experimental run. It is noted that the values of wall shear stress reported by Wilson (2011) for the analysis of this particular experimental run were about an order of magnitude too small.

The pipe discharges computed with the CFD simulation, the time required for the pipe to erode to a given pipe radius, the calculated Darcy–Weisbach discharge, the average wall shear stress, and the average suspended sediment concentration in the pipe discharge are presented in Table 2. This table also summarizes the results for the case of a rough pipe wall, which is presented below. The change in pipe discharge and pipe discharge suspended sediment concentration with time calculated from the model is presented along with the observed data in Fig. 6a.

The modeled pipe discharge varied from 46 L h^{-1} for the initial diameter of 6 mm to 2435 L h^{-1} for the final pipe diameter of 24 mm. As shown in Table 2, these discharge values are reasonably close to values calculated using the Darcy–Weisbach equation for full-pipe flow. However, comparison of simulated pipe discharges with measured discharges show that the simulated values significantly overpredict the observed values starting at about 1000 s into the experiment, corresponding to the time when the average pipe diameter should be about 13 mm.

The modeled pipe suspended sediment concentrations at the outlet of the pipe are provided in Table 2 and plotted in Fig. 6a. It can be observed that the predicted concentrations are far below the measured concentrations at early time but then match the concentrations after about 600 s and beyond into the experiment. The reason for the low concentrations early in the simulation have to do with the use of a constant value of k_{eros} for the simulations. Calculating k_{eros} using the experimental data collected by Wilson

Table 1. Parameters set for the numerical solution of the flow and transport equations.

Pipe condition	α^\dagger	σ_ω	σ_k	$\beta_{\omega,o}$	$\beta_{k,o}$	Soil erodibility coefficient k_{eros}	Critical wall shear stress τ_{crit}	Fluid density ρ	Fluid dynamic viscosity μ	Relative roughness ε/D	Turbulent diffusion coefficient D_T
						s m^{-1}	Pa	kg m^{-3}	Pa s		$\text{m}^2 \text{s}^{-1}$
Smooth wall	0.52	0.5	0.5	0.133	0.166	0.00195	0.005	999.6	0.001	0.00	5×10^{-4}
Rough wall	0.52	0.5	0.5	0.133	0.166	0.0025	0.005	999.6	0.001	$(\varepsilon/D)^\ddagger$	5×10^{-4}

$^\dagger \alpha, \sigma_\omega, \sigma_k, \beta_{\omega,o}, \text{ and } \beta_{k,o}$ are dimensionless parameters in the Reynolds-averaged Navier–Stokes equations.

‡ The surface roughness is dependent on pipe radius and is calculated from Eq. [14].

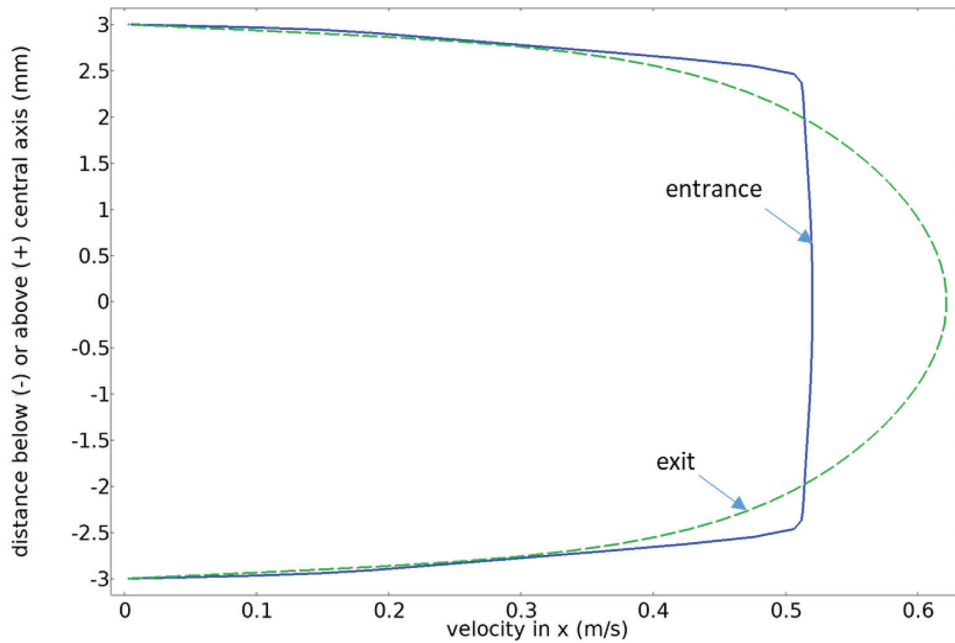


Fig. 4. Velocity distribution across the section of the 6-mm-diameter soil pipe at the entrance and the exit of the pipe for the case of smooth-walled pipe at the time of flow initiation ($t = 0$ s). The solid line is for the pipe entrance and the broken line is for the pipe exit.

(2011) showed that the value had a large range between 0.0074 and 0.0006 s m^{-1} . The details of the calculation of this parameter from the experimental data, and implications of the temporal variation in this parameter, are presented in the Discussion section.

The modeled wall shear stress values presented in Table 2 are between 1.5 and 3.5 % less than the values that would occur if one calculates the wall shear stress with $\tau_w = \rho g H r_p / 2L$. The reason for this discrepancy is that this formula assumes that the velocity profile is fully developed in the pipe. For that assumed condition, the wall shear just balances the applied pressure difference. In the case where the velocity profile develops within the length of the pipe, part of the pressure difference assists with the acceleration of the water within the pipe. Based on the principle of linear momentum balance, this means that the

wall shear will be somewhat less than that calculated with the above formula.

To reduce the simulated pipe discharges to values more in line with the measured discharges, the walls of the pipe were treated as being rough. Incorporating the wall roughness may be justified on the basis of the fact that the pipe diameter was found to be quite non-uniform as measured at the end of the experiment (Fig. 2). Wilson (2011) reported that the mean final diameter of the soil pipe was 23.8 mm with a coefficient of variability of 0.26. This variability in pipe diameter was used as a measure of the macroscopic roughness of the pipe wall rather than directly modeling the actual spatial variation in pipe diameter.

Utilizing these rough wall conditions, the simulations were repeated, assigning a relative wall roughness given by

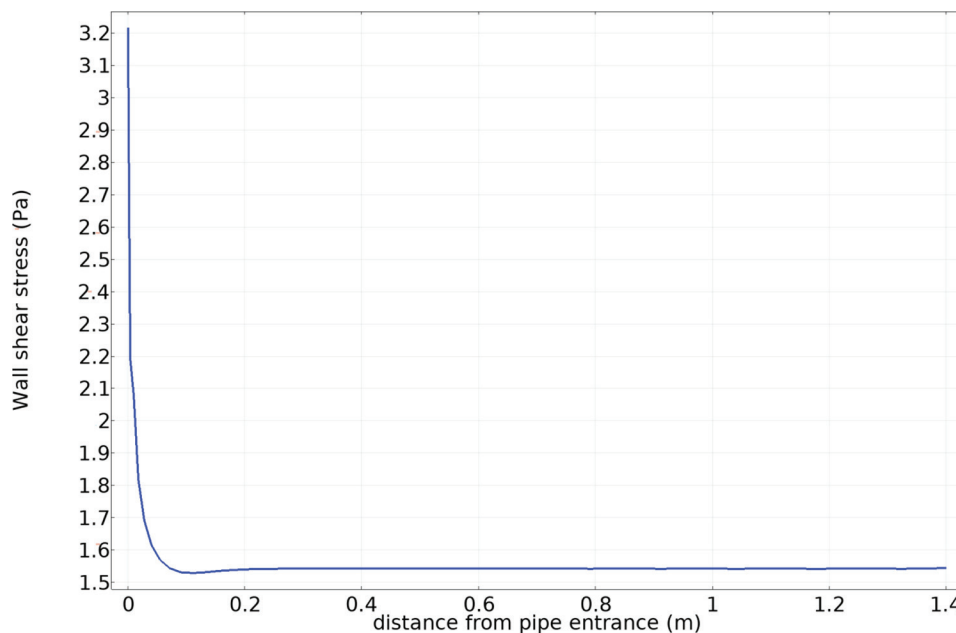


Fig. 5. Shear stress on the wall of the soil pipe along its length for the soil pipe when it was 6 mm in diameter, which occurred at flow initiation ($t = 0$ s).

Table 2. Pipe flow, mean wall shear stress, and suspended sediment concentration for the case of a smooth walled pipe, and a rough walled pipe.

Pipe diam.	Smooth wall					Rough wall				
	Pipe flow†	Time to reach diam.	Pipe flow, Darcy–Weisbach‡	Mean wall shear	Suspended sediment conc.	Pipe flow†	Time to reach diam.	Pipe flow, Darcy–Weisbach‡	Mean wall shear	Suspended sediment conc.
mm	L h ⁻¹	s	L h ⁻¹	Pa	g L ⁻¹	L h ⁻¹	s	L h ⁻¹	Pa	g L ⁻¹
6	46	0	55	1.55	6.3§	46	0	55	1.55	8.0¶
8	106	379	122	2.06	4.8	97	310	103	2.0	6.3
12	341	895	373	3.08	3.3	264	778	243	2.81	4.6
16	780	1269	816	4.08	2.6	498	1161	488	3.58	3.8
20	1455	1561	1495	5.07	2.2	775	1502	719	4.07	3.3
24	2435	1803	2447	6.08	1.9	1045	1828	1057	4.52	3.0

† Computational fluid dynamics model results.

‡ Discharge calculated with the Darcy–Weisbach equation for full pipe flow.

§ Value is calculated with $k_{\text{eros}} = 0.00195 \text{ s m}^{-1}$.

¶ Value is calculated with $k_{\text{eros}} = 0.0025 \text{ s m}^{-1}$.

$$\frac{\varepsilon}{D} = 0.13 \left(\frac{r_p - 0.003}{0.009} \right) \quad [14]$$

This expression yields a wall roughness of zero initially ($t = 0$), which then increases in direct proportion to the pipe radius such that at the largest pipe diameter, 24 mm, the wall roughness is 3.12 mm. The parameter settings for the rough-walled pipe case are summarized in Table 1.

The resulting simulations for pipe flows are presented in Table 2. The simulated pipe discharges are again reasonably close to discharges calculated using the Darcy–Weisbach equation. For the simulation of the pipe erosion rate, the erodibility coefficient was set by trial and error to 0.0025 s m^{-1} . This was the value that yielded a simulated pipe growth evolution similar to that observed in the experiment. Similar to what was observed for the case of the smooth pipe, this calibrated value of the erodibility coefficient was again about 1/20 the value reported by Wilson (2011). A plot of the simulated pipe discharge and outflow sediment concentration along with the observed values is shown in Fig. 6b. There is excellent agreement between the observed and simulated pipe discharges. However, as with the smooth-wall pipe simulations, the suspended sediment concentrations again fall below the measured values until about 600 s. As mentioned above for the smooth-wall pipe simulations, the implications of using the constant value of k_{eros} in the simulations is presented in the Discussion section.

One additional test of the pipe discharge simulations was conducted to assess the effect of pipe diameter variability on pipe flow. For this, a geometric model was constructed to match the geometry of the pipe as measured at the end of the experiment. This geometric model is illustrated in Fig. 7.

The CFD model was run using the same boundary conditions as those applied for the uniform diameter pipe configurations. For this non-uniform pipe case, the walls were treated as being smooth. The results of the numerical simulation

yielded a pipe discharge of 1112 L h^{-1} . Note that the measured discharge was reported by Wilson (2011) to be 1200 L h^{-1} , which compares fairly well with the simulated discharge. We consider this level of agreement between the measured discharge and the simulated discharge for the non-uniform pipe to be confirmation of the CFD solution.

Discussion

Assumption of Steady-State Transitions

In this study, we assumed that the growth of the pipe diameter could be simulated by taking a series of steady-state flow and transport configurations and linking those via a simple integration of mass lost and pipe growth with time. An alternative to this approach would be to solve the time-dependent flow and sediment erosion and transport equations, which would then require implementation of dynamic meshing within the framework of the solution. The approach used here and the dynamic approach should yield identical results if the pipe diameter increment used for the steady-state approach is made small enough. COMSOL-MP (COMSOL, 2018) does facilitate the full dynamic approach; however, implementation of it is left to future efforts.

Assumption of Uniform Pipe Growth

We assumed that the pipe diameter grows uniformly along the length of the pipe. While the simulated shear stress on the pipe wall was essentially uniform across 75 to 90% of the pipe length, the wall shear stress is much higher near the pipe entrance and decreases rapidly to the constant value across the first 10 to 25% of the pipe length. Because the pipe erosion rate, and thereby the pipe diameter growth, are both tied directly to the wall shear stress, the non-uniformity of the wall shear stress should prompt the use of a non-uniform pipe growth rate and therefore a pipe with non-uniform diameter. However, to keep the analysis somewhat simpler, we decided to work

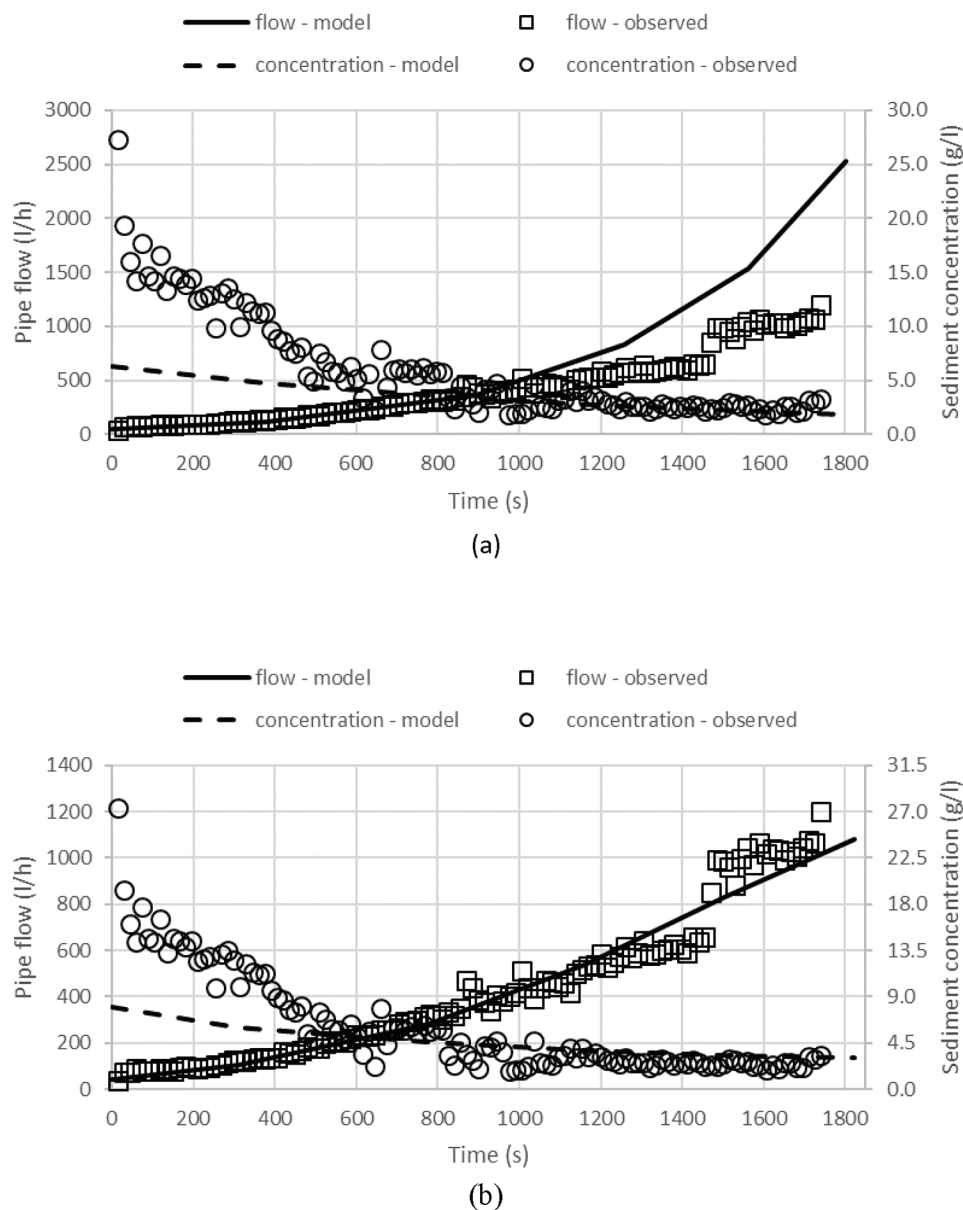


Fig. 6. Simulated and observed pipe flow and suspended sediment concentrations vs. time for two simulation cases: (a) for the case of smooth walls, and (b) for the case with rough walls.

with the pipe configuration having a uniform diameter for this initial study.

In this study, the pipe flow simulations essentially matched the measured pipe flow when wall roughness was included in the flow simulations. The variations in pipe diameter measured at the end of the experiment were used to quantify the relative roughness of the pipe wall. A better way to treat the flow simulation would be to use the non-uniform pipe flow sections directly in formulating the geometry of the flow domain and then add on top of that some wall roughness to account for the size of soil particles or for deposits of particles on the wall surface.

Critical to future work on this topic is the need to address the question of what causes the pipe growth to be non-uniform and non-monotonic with regard to distance along the pipe. A few

factors come to mind when considering this, including the non-uniformity of wall shear stress, deposition of particles onto pipe walls, and non-uniformity of wall shear strength.

Assumption of Constant Soil Erodibility Coefficient

For the experiment reported by Wilson (2011), water samples were collected every 15 s for the duration of the experiment. Sediment concentrations were measured for those samples, and from those measurements the sediment flux rate was determined. The coefficient, k_{eros} , can be calculated using the experimental data and the following equation (derived from manipulation of Eq. [9] and [11]):

$$k_{eros} = \frac{\bar{Q}_s}{2\pi\bar{r}_p L(\bar{\tau}_w - \tau_c)} \quad [15]$$

where \bar{Q}_s , \bar{r}_p , and $\bar{\tau}_w$ are the average sediment discharge, average pipe radius, and average wall shear stress over a time interval Δt , respectively. Assuming the velocity profile is fully developed along the entire length of the pipe, the wall shear stress term is calculated as $\bar{\tau}_w = \rho g H \bar{r}_p / 2L$. The results of the analysis yielded values of k_{eros} ranging from 0.0074 to 0.0006 s m⁻¹. A plot of the results is shown in Fig. 8, showing that the coefficient decreases exponentially from the initial value of 0.0074 s m⁻¹.

In the numerical simulations of the erosion of the pipe walls, it was assumed that k_{eros} was constant for

the entire period of the simulation. However, the experimental evidence illustrated in Fig. 8 indicates that k_{eros} is variable. Equation [9] is a semi-empirical equation, and as such it does not fully describe the erosion rate based on physics and therefore has its limitations. The fact that k_{eros} appears to be a function of the shear stress means that a more complete, physically based erosion model needs to be adopted to be able to capture the dynamics of pipe erosion.

To demonstrate the efficacy of using a variable k_{eros} in the numerical solution, the value was set to 0.0074 s m⁻¹ for the initial phase ($t = 0$). The numerical solution yielded a suspended sediment concentration of 23.4 g L⁻¹ at $t = 0$ s. Referring to Fig. 6b, the measured suspended sediment concentration at the start of the experiment had a concentration of about 27 g L⁻¹.

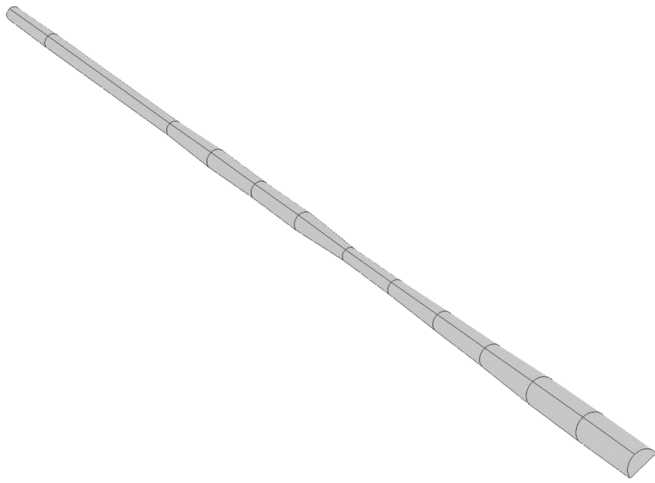


Fig. 7. Image of the representation of the nonuniform diameter pipe as measured at the end of the experiment. The pipe domain was constructed from the data presented in Fig. 2. The lower right is the pipe entrance, and the upper left is the pipe exit. This domain was used in simulation of the flow that was measured near the end of the experiment.

Additional work will need to be done to include a time-varying k_{eros} in the simulation. This would require adjustments of the time variation of the pipe growth consistent with the variations in erosion rate. With the combination of the measured pipe discharge and suspended sediment concentration there is enough information to derive the appropriate time-varying k_{eros} . However, this was not attempted in the present study and is left to future efforts.

Other Considerations

The flow of water in soil pipes, the detachment of soil particles off soil pipe walls, and the transport of detached particles

through the length of a soil pipe is a complex process. In this study, we imposed a number of assumptions, in addition to those discussed above, that made the modeling more tractable within the present effort. The assumptions include: (i) no interaction between suspended particles; (ii) no deposition of suspended particles; (iii) no influence of suspended particles on fluid properties; (iv) no effect of particle collision with the pipe wall on particle detachment; (v) a linear relationship between wall shear stress and detachment rate as expressed by Eq. [9]; and (vi) infiltration of water from the pipe into the surrounding media was neglected.

Lahiri and Ghanta (2010) and Bello et al. (2011) both conducted modeling studies to examine the transport of solid particles in oil pipeline systems, having an interest in either knowing how the transported particles affect the energy loss associated with the fluid flow or to examine the effect of solid collision with pipe boundaries on pipe corrosion. Both studies were not limited by assumptions (i) to (iv). The approaches given in those studies should be adopted in the future to improve the ability to model the erosion and sediment transport in soil pipes.

The fifth item might be addressed using an alternative particle detachment model. An example of a more phenomenological approach to computing particle detachment is the equation proposed by Wilson (1993).

It is expected that the loss of water entering the soil pipe to the soil matrix surrounding the soil pipe will be small compared with the flow through the soil pipe. As an example quantification of this, if the hydraulic conductivity of the soil is assumed to be $3.5 \times 10^{-5} \text{ m s}^{-1}$ (medium sand), the infiltration into the soil along the full length of the pipe for a pipe diameter of 24 mm will be about 13 L h^{-1} , a value much smaller than the flow through the pipe. This justifies assumption (vi).

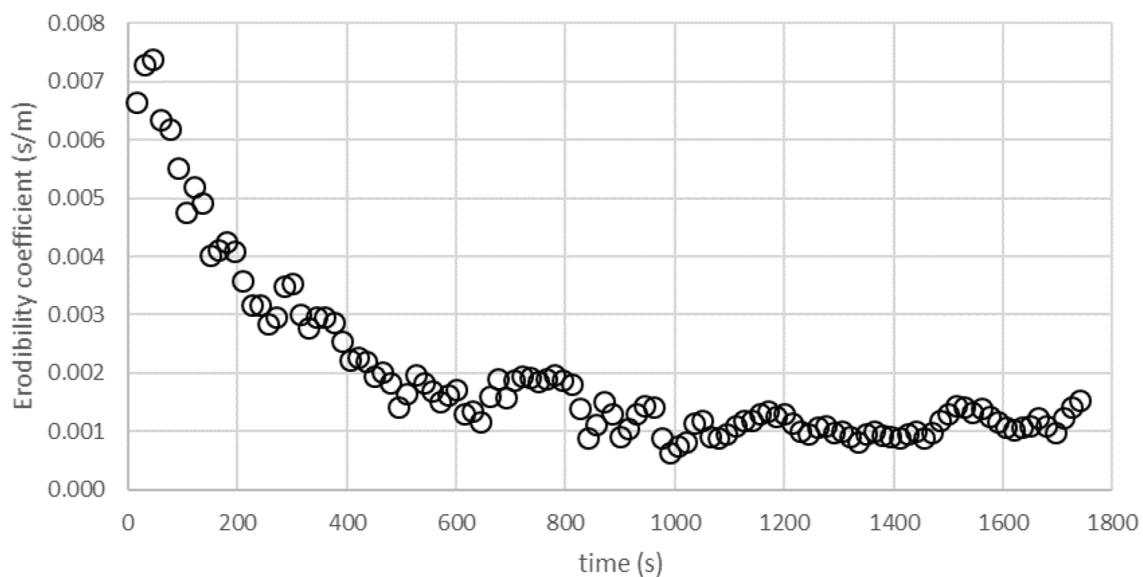


Fig. 8. Erodibility coefficient vs. time calculated using sediment flux data reported by Wilson (2011) for the soil pipe experiment with Providence soil and an initial pipe diameter of 6 mm.

Conclusions

A k - ω turbulence model for the Reynolds-averaged Navier–Stokes equations has been successfully coupled with the governing equation for transport of suspended sediment to simulate the internal erosion of a uniform diameter, straight soil pipe. Simulations were performed with initial conditions and boundary conditions related to a laboratory experiment reported by Wilson (2011). The boundary condition for flow was a constant pressure head applied at the pipe inlet and zero pressure head at the pipe outlet. Fluid shear on the wall of the soil pipe led to wall erosion and pipe diameter growth with time. The growth of the pipe was modeled assuming steady-state flow conditions within each of a sequence of increasing pipe diameters. Pipe growth was then modeled by a simple mass balance equation for the eroded soil.

A major limitation identified in the study was the assumption that the pipe remained uniform in diameter along its length during the erosion process. Measurements of the pipe diameter at the end of the experiment discussed here, as reported by Wilson (2011), showed that the coefficient of variation in pipe diameter was 26%. This non-uniformity in pipe diameter should increase the resistance to flow in the pipe and thereby decrease the flow capacity. This roughness will also affect the wall shear and may affect the erodibility coefficient needed to match the measured pipe erosion rate. Important parameters for the flow and erosion modeling included the internal roughness of the pipe wall and the erodibility coefficient. It was found that when assuming the pipe walls to be smooth, the simulated pipe discharge was too high by more than a factor of two compared with measurements. Specifying pipe wall roughness, based on laboratory-measured pipe diameter variations, led to a reduction of flow to levels corresponding to those measured in the laboratory. A constant soil erodibility coefficient of 0.0025 s m^{-1} for the case of a rough-walled soil pipe yielded erosion rates leading to an appropriate pipe growth rate and sediment concentrations matching the late-time experimental measurements. A time-varying soil erodibility coefficient is suggested to more accurately simulate the sediment concentrations measured over the duration of the experiment.

To better simulate the observed soil pipe erosion, it will be necessary to incorporate some improvements in the modeling approach, and several suggestions are enumerated here. These suggestions include:

1. Implement the full dynamics of pipe growth into the fluid flow and soil erosion and sediment transport model.
2. Include the particle–particle and fluid–particle interactions into the sediment transport equations and the fluid–particle interactions into the fluid flow equations.
3. Include the influence of suspended sediment concentration on fluid properties.
4. Evaluate an alternative to the excess shear stress equation for particle detachment, e.g., the equation by Wilson (1993).

Variables and Parameters

\bar{c}	time-averaged suspended sediment concentration (g L^{-1})
D_T	turbulent dispersion coefficient ($\text{m}^2 \text{ s}^{-1}$)
\mathbf{g}	vector of gravitational acceleration composed of components g_x , g_y , and g_z (m s^{-2})
\mathbf{I}	identity matrix
k	specific turbulent kinetic energy ($\text{m}^2 \text{ s}^{-2}$)
k_{eros}	soil erodibility coefficient (s m^{-1})
L	length of the soil pipe (m)
p	fluid pressure (Pa)
\bar{p}	time-averaged pressure (Pa)
p_ϕ	turbulent component of fluid pressure (Pa)
P_k	production rate for turbulent kinetic energy (W m^{-3})
q_s	pipe wall erosion rate ($\text{kg m}^{-2} \text{ s}^{-1}$)
\bar{Q}_s	sediment discharge measured in the experiment (kg s^{-1})
r_p	pipe radius (m)
$\bar{u}_{x\delta}$	velocity at the interface between the turbulent boundary layer and the laminar sublayer (m s^{-1})
$\bar{u}_{x\text{ls}}$	velocity in the laminar sublayer (m s^{-1})
\mathbf{V}	vector of velocity composed of components u_x , u_y , u_z (m s^{-1})
$\bar{\mathbf{V}}$	vector of time-averaged velocity, composed of components \bar{u}_x , \bar{u}_y , \bar{u}_z (m s^{-1})
\mathbf{V}'	vector of turbulent velocity, composed of components u_x' , u_y' , u_z' (m s^{-1})
δ	thickness of laminar sublayer (m)
μ	dynamic viscosity of the fluid (Pa s)
μ_T	turbulent viscosity (Pa s)
ρ	fluid density (kg m^{-3})
ρ_d	dry bulk density of the soil (kg m^{-3})
τ_{crit}	critical wall shear stress (Pa)
τ_w	wall shear stress (Pa)
ω	specific dissipation rate of turbulent kinetic energy (m s^{-1})
α , σ_ω , σ_k , $\beta_{k,0}$, and $\beta_{\omega,0}$	are dimensionless turbulent flow parameters

Acknowledgments

We wish to thank Peter Germann and an anonymous reviewer for their careful and helpful reviews of this manuscript. J.L. Nieber's effort on this project was partially supported by the USDA National Institute of Food and Agriculture, Hatch/Multistate Project MN 12-059.

References

- Bello, O., G. Falcone, C. Teodoriu, and I. Udong. 2011. A mechanistic model for predicting for predicting oil-sand flow in horizontal wells. *Oil Gas Sci. Technol.* 66:979–989. doi:10.2516/ogst/2010034
- Bernatek-Jakiel, A., M. Jakiel, and K. Kreemien. 2017. Piping dynamics in mid-altitude mountains under a temperate climate: Bieszczady Mts., Eastern Carpathians. *Earth Surf. Processes Landforms* 42:1419–1433. doi:10.1002/esp.4160
- Bernatek-Jakiel, A., and J. Poesen. 2018. Subsurface erosion by soil piping: Significance and research needs. *Earth-Sci. Rev.* 185:1107–1128. doi:10.1016/j.earscirev.2018.08.006
- Beven, K.J., and P.F. Germann. 1982. Macropores and water flow in soils. *Water Resour. Res.* 18:1311–1325. doi:10.1029/WR018i005p01311
- Beven, K.J., and P.F. Germann. 2013. Macropores and water flow in soils revisited. *Water Resour. Res.* 49:3071–3092. doi:10.1002/wrcr.20156

- COMSOL. 2018. COMSOL Multiphysics 5.4. CFD module, user's guide. COMSOL, Burlington, MA.
- Fox, G.A., and G.V. Wilson. 2010. The role of subsurface flow in hillslope and streambank erosion: A review of status and research needs. *Soil Sci. Soc. Am. J.* 74:717–733. doi:10.2136/sssaj2009.0319
- Gerke, H.H. 2006. Preferential flow descriptions for structured soils. *J. Plant Nutr. Soil Sci.* 169:382–400. doi:10.1002/jpln.200521955
- Gerke, H.H., and M.Th. van Genuchten. 1993. A dual-porosity model for simulating the preferential movement of water and solutes in structured porous media. *Water Resour. Res.* 29:305–319. doi:10.1029/92WR02339
- Haaland, S.E. 1983. Simple and explicit formulas for the friction-factor in turbulent pipe flow. *J. Fluids Eng.* 105:89–90. doi:10.1115/1.3240948
- Jarvis, N.J. 2007. A review of non-equilibrium water flow and solute transport in soil macropores: Principles, controlling factors, and consequences for water quality. *Eur. J. Soil Sci.* 58:523–546. doi:10.1111/j.1365-2389.2007.00915.x
- Jones, J.A.A. 2010. Soil piping and catchment response. *Hydrol. Processes* 24:1548–1566. doi:10.1002/hyp.7634
- Lahiri, S.K., and G.C. Ghanta. 2010. Slurry flow modeling by CFD. *Chem. Ind. Chem. Eng. Q.* 16:295–308. doi:10.2298/CICEQ091030031L
- Munson, B.R., T.H. Okiishi, W.W. Huebsch, and A.P. Rothmayer. 2013. *Fundamentals of fluid mechanics*. 7th ed. John Wiley & Sons, Hoboken, NJ.
- Nieber, J.L., and R.C. Sidle. 2010. How do disconnected macropores in sloping soils facilitate preferential flow? *Hydrol. Processes* 24:1582–1594. doi:10.1002/hyp.7633
- Partheniades, E. 1965. Erosion and deposition of cohesive soils. *J. Hydraul. Div., Am. Soc. Civ. Eng.* 91:105–139.
- Sidle, R.C., H. Kitahara, T. Terajima, and Y. Nakai. 1995. Experimental studies on the effects of pipeflow on throughflow partitioning. *J. Hydrol.* 165:207–219. doi:10.1016/0022-1694(94)02563-Q
- Sidle, R.C., S. Noguchi, Y. Tsuboyama, and K. Laursen. 2001. A conceptual model of preferential flow systems in forested hillslopes: Evidence of self-organization. *Hydrol. Processes* 15:1675–1692. doi:10.1002/hyp.233
- Wan, C.F., and R. Fell. 2004. Laboratory test on the rate of piping erosion of soils in embankment dams. *Geotech. Test. J.* 27:295–303.
- Wanger, M., G.A. Fox, G.V. Wilson, and J. Nieber. 2019. Laboratory experiments on the removal of soil plugs during soil piping and internal erosion. *Trans. ASABE* 62:83–93. doi:10.13031/trans.13092
- Wilcox, D.C. 2006. *Turbulence modeling for CFD*. 3rd ed. DCW Industries, La Cañada, CA.
- Wilcox, D.C. 2008. Formulation of the k - ω turbulence model revisited. *AIAA J.* 46:2823–2838. doi:10.2514/1.36541
- Wilson, B.N. 1993. Development of a fundamental based detachment model. *Trans. ASAE* 36:1115–1122. doi:10.13031/2013.28442
- Wilson, G.V. 2009. Mechanisms of ephemeral gully erosion caused by constant flow through a continuous soil-pipe. *Earth Surf. Processes Landforms* 34:1858–1866. doi:10.1002/esp.1869
- Wilson, G.V. 2011. Understanding soil-pipe flow and its role in ephemeral gully erosion. *Hydrol. Processes* 25:2354–2364. doi:10.1002/hyp.7998
- Wilson, G.V., and G.A. Fox. 2013. Pore-water pressures associated with clogging of soil pipes: Numerical analysis of laboratory experiments. *Soil Sci. Soc. Am. J.* 77:1168–1181. doi:10.2136/sssaj2012.0416
- Wilson, G.V., J.L. Nieber, G.A. Fox, S.M. Dabney, M. Ursic, and J.R. Rigby. 2017. Hydrologic connectivity and threshold behavior of hillslopes with fragipans and soil pipe networks. *Hydrol. Processes* 31:2477–2496. doi:10.1002/hyp.11212
- Wilson, G.V., J.L. Nieber, R.C. Sidle, and G.A. Fox. 2013. Internal erosion during soil pipeflow: State of the science for experimental and numerical analysis. *Trans. ASABE* 56:465–478. doi:10.13031/2013.42667
- Wilson, G.V., J.R. Rigby, M. Ursic, and S.M. Dabney. 2016. Soil pipe flow tracer experiments: 1. Connectivity and transport characteristics. *Hydrol. Processes* 30:1265–1279. doi:10.1002/hyp.10713
- Wilson, G.V., R.R. Wells, R. Kuhnle, G.A. Fox, and J. Nieber. 2018. Sediment detachment and transport processes associated with internal erosion of soil pipes: State of science. *Earth Surf. Processes Landforms* 43:45–63. doi:10.1002/esp.4147
- Zhou, Y., G.V. Wilson, G.A. Fox, J.R. Rigby, and S.M. Dabney. 2016. Soil pipe tracer experiments: 2. Application of a streamflow transient storage zone model. *Hydrol. Processes* 30:1280–1291. doi:10.1002/hyp.10712